Manipulation and Characterization of the Valley-Polarized Topological Kink States in Graphene-Based Interferometers

Shu-guang Cheng,[1,2] Haiwen Liu,[3] Hua Jiang,[4,5,*] Qing-Feng Sun,[6,7,8,†] and X. C. Xie[6,7,8]
[1]Department of Physics, Northwest University, Xi'an 710069, China
[2]Shaanxi Key Laboratory for Theoretical Physics Frontiers, Xi'an 710069, China
[3]Center for Advanced Quantum Studies, Department of Physics, Beijing Normal University, Beijing 100875, China
[4]School of Physical Science and Technology, Soochow University, Suzhou 215006, China
[5]Institute for Advanced Study, Soochow University, Suzhou 215006, China
[6]International Center for Quantum Materials, School of Physics, Peking University, Beijing 100871, China
[7]Collaborative Innovation Center of Quantum Matter, Beijing 100871, China
[8]CAS Center for Excellence in Topological Quantum Computation, University of Chinese Academy of Sciences, Beijing 100190, China

(Received 10 May 2018; published 8 October 2018)

Valley polarized topological kink states, existing broadly in the domain wall of hexagonal lattice systems, are identified in experiments. Unfortunately, only very limited physical properties are given. Using an Aharanov-Bohm interferometer composed of domain walls in graphene systems, we study the periodical modulation of a pure valley current in a large range by tuning the magnetic field or the Fermi level. For a monolayer graphene device, there exists one topological kink state, and the oscillation of the transmission coefficients has a single period. The π Berry phase and the linear dispersion relation of kink states can be extracted from the transmission data. For a bilayer graphene device, there are two topological kink states with two oscillation periods. Our proposal provides an experimentally feasible route to manipulate and characterize the valley-polarized topological kink states in classical wave and electronic graphene-type crystalline systems.

DOI: 10.1103/PhysRevLett.121.156801

Introduction.—Topological kink states broadly exist in the domain walls of magnetic topological insulators [1,2], electronic graphene-type systems [3–7], and classical wave graphene systems [8–14]. Aside from the theoretical studies of kink states in bilayer graphene [3,15–20], recent experimental observations have generated great interest in exploring the exotic properties of such states [5,6,21–23]. However, the kink states are restricted to a very narrow region, which makes it rather difficult to characterize with common techniques, such as angle resolved photoemission spectroscopy. At the present, the approaches of STM, transport, and infrared measurement can only prove the existence of a kink state. The pseudospin-momentum locking property, the band structure, and even the number of kink states have not been determined experimentally. Similar problems also exist in topological insulators [1,2], the graphenelike classical wave systems [8–14], and MoS_2 [24].

The valley-polarized states can be used for fabricating valley filter, a key device for valleytronics applications [25–29]. The domain walls in graphene systems, which host valley-polarized topological kink states, can serve as valley filters [27,28]. Nevertheless, in a single domain wall the valley current cannot be easily manipulated. Based on a current splitter [30,31] composed of two crossed domain walls, the current partition rule of the kink state is investigated, indicating the manipulation of valley-polarized kink states through a splitter [32,33]. The control of current in such a splitter is still difficult since the morphology of the domain wall is unchangeable when the device is fabricated, thus prohibiting the manipulation of the kink states.

For the applications of valleytronics, the manipulation of valley-polarized current conveniently is essential. Very recently, domain networks in bilayer graphene have been observed experimentally [34,35], which makes the interference of the kink states possible. We adopt this platform for the characterization and manipulation of kink states through quantum interference.

In this Letter, we study the quantum interference of the Aharanov-Bohm (AB) interferometer [34,36] composed of topological kink states locating at the domain walls of graphene systems (see Fig. 1). Both the magnetic field and the gate voltage can be utilized to manipulate these kink states, in which only the valley-polarized current is allowed for propagation and interference. The magnitude of the valley-polarized current can be adjusted periodically in a wide range by varying the Fermi energy or a magnetic field. The number of kink states can be obtained from the oscillation pattern of the transmission coefficients. For a monolayer graphene interferometer, there is one kink state and one oscillation period, while for a bilayer graphene system, two kink states and two periods exist. Specifically

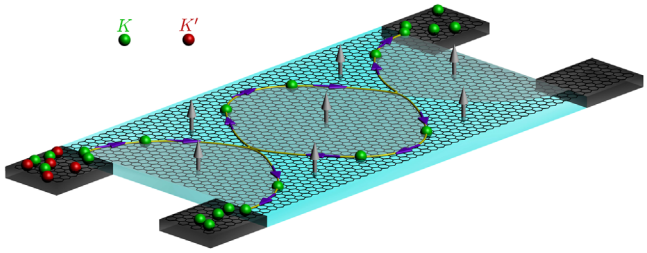

FIG. 1. Schematic view of the kink state interferometer under the magnetic field. Four terminals are attached to the central region. In the central region, the domain walls (yellow paths) are defined by the lines across which the sign of mass term in graphene reverses. The purple arrows indicate the propagation direction of the valley K electrons, and the gray vertical arrows stand for the magnetic field.

for the former case, a π Berry phase and a linear band structure of the kink state can be obtained from the transport data. The exotic kink states can broadly exist in graphene-type systems, including their classical wave cousins [8–14], and thus can be realized in the present experiments.

Model and methods.—Four-terminal graphene-nanoribbon-based devices with a single splitter [see Figs. 2(a) and 2(b)] or two splitters [see Fig. 1] are investigated. Under a small voltage bias between terminal 1 and the other terminals, only electrons of valley K can flow from terminal 1 into the central region. In the tight-binding representation, the model Hamiltonian reads [18,28]

$$H_m = \sum_i \varepsilon_i c_i^\dagger c_i + \sum_{\langle ij \rangle} t(e^{i\phi_{ij}} c_i^\dagger c_j + e^{-i\phi_{ij}} c_j^\dagger c_i), \quad (1)$$

where $c_i^\dagger$ and c_i are the creation and annihilation operators of electrons at site i, respectively. In the four terminals, the on-site potential is $\epsilon_i = V$; thus, the neutral point is shifted by

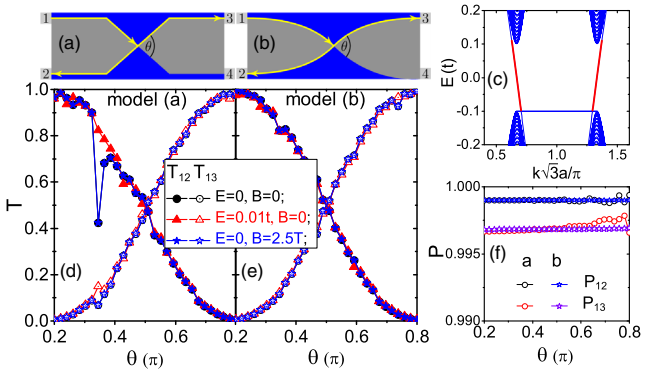

FIG. 2. Schematics for two types of kink state splitter: straight line (a) and cosine (b) shaped. (c) Band structures for kink states in monolayer graphene model. (d),(e) Angle θ dependence of T_{12} and T_{13} for model (a) and (b) for different E and B, respectively. (f) θ dependence of valley polarization of T_{12} and T_{13} when $E = 0$, $B = 0$ for model (a) and (b). The devices' width is $L = 600a$.

the gate voltage V. It guarantees that in the terminals there are dozens of states for each valley at the Fermi level [37]. In the central region, ε_i defines the domain walls [4,28]. For monolayer graphene, there are two set of sublattices, namely, A and B. In the blue (gray) region [see Figs. 2(a) and 2(b)], $\varepsilon_A = U(-U)$ and $\varepsilon_B = -U(U)$. The second term represents the nearest-neighbor coupling with energy t. The uniform perpendicular magnetic field exists only in the central region and is accounted for by the phase factor ϕ_{ij}.

Adopting the transfer matrix method, the transmission coefficients are calculated [29,38]. Following the standard procedure, each transmission coefficient t_{mn}^{ij} from state i in terminal m to state j in terminal n is obtained. The valley-resolved transmission coefficients are accessed by collecting t_{mn}^{ij} in two separate valleys (K and K'): $T_{mn}^{K_1K_2}(E,B) = \sum_{i\in K_1}\sum_{j\in K_2} t_{mn}^{ij}$, with E the Fermi energy and B the magnetic field. The total transmission coefficient is $T_{mn} = T_{mn}^{KK} + T_{mn}^{KK'} + T_{mn}^{K'K} + T_{mn}^{K'K'}$, and the corresponding valley polarization is $P_{mn} = (T_{mn}^{KK} + T_{mn}^{KK'} - T_{mn}^{K'K} - T_{mn}^{K'K'})/T_{mn}$. In the numerical calculation we use $U = 0.1t$ and $V = 0.2t$, with t the energy unit in Eq. (1). Under the gauge transformation, the magnetic field B is related to ϕ by $B = 2h\phi/3\sqrt{3}a^2\pi e$ with a the C—C bond length. At zero temperature, the current I_{mn} is proportional to T_{mn} due to the Landauer-Buttiker formula, so we are only concerned with T_{mn} in the following discussion.

Single splitter.—The band structure of the kink states for the monolayer graphene model is displayed in Fig. 2(c). The propagation direction of the kink state of different valleys is opposite to each other. First, the transport of the kink states in devices with a single splitter, shown in Figs. 2(a) and 2(b), is investigated. Current injected from terminal 1 can only transmit into terminals 2 and 3. Note that in the domain wall near terminal 2, the current is of valley K, too, because the energy band is reversed [15]. We find $T_{12} + T_{13} \simeq 1$ [see Figs. 2(d) and 2(e)] due to the valley conservation, and both T_{12} and T_{13} are high valley polarized [see Fig. 2(f)], signaling that the nearly pure valley currents are obtained in terminals 2 and 3. In the following, we discuss only the magnitudes of the transmission coefficients. The angle-dependent partition rule in Ref. [32] is reproduced in Figs. 2(d) and 2(e) with nonzero E and B. For a smooth splitter, the partition of the valley current is determined by the intersection angle at the cross point and is insensitive to the Fermi level (near the neutral points), the weak magnetic field, and the specific line shape of the splitter.

Monolayer graphene interferometer.—Now we focus on the interferometer formed by domain walls with two splitters, as shown in Fig. 3(a). The incoming wave from terminal 1, at the left splitter, is partitioned to terminal 2 and the upper arm of the interferometer. At the right splitter, again the wave is split into terminal 3 and the lower arm. Then the wave along the lower arm meets the first splitter

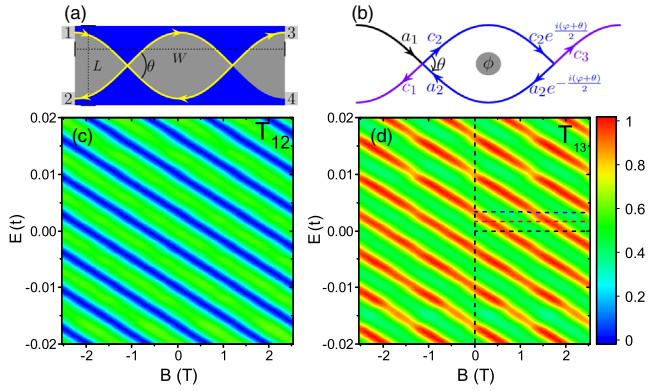

FIG. 3. Schematic of the kink state interferometer (a) and wave propagation (b). Two-dimensional map of E and B dependence of T_{12} (c) and T_{13} (d). The sample sizes are $L = 600a$ and $W = 600\sqrt{3}a$.

and is split for the third time. The process happens repeatedly and the current flow into terminal 2 or terminal 3 results from the multibeam interference. The Fermi level E and magnetic field B dependence of $T_{13}(E, B)$ are shown in Figs. 3(c) and 3(d). Also, $T_{12} + T_{13} \simeq 1$ due to the weak backscattering. Significantly, both T_{12} and T_{13} are modulated by B and E periodically in a wide range (e.g., $T_{13}^{\max/\min} = 0.93/0.41$ corresponds to $T_{12}^{\min/\max} = 0/0.57$). Note that both T_{12} and T_{13} are nearly valley polarized, so the device is a well controllable valley filter.

The details of T_{13} are displayed in Figs. 4(a) and 4(b). In Fig. 4(a), two main characteristics are observed: (i) T_{13} shows a minimum at $B = 0$ and $E = 0$, and (ii) the oscillation of $T_{13}(E_i, B)$ versus B is shifted periodically as E_i changes. The magnetic flux enclosed by the interferometer (from the period of T_{13}) is about h/e, indicating the good performance of the AB interferometer. To understand the characteristics better, the redistribution of valley K electrons from terminal 1 in the interferometer is pictured

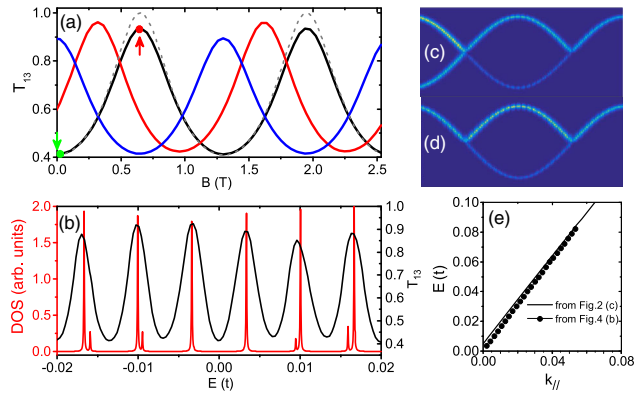

FIG. 4. (a) B and (b) E dependence of T_{13} along the dashed lines in Fig. 3(d). The dashed curve in (a) is from Eq. (2). The red curve in (b) is the DOS of an isolated kink state circle. (c),(d) $\rho(\mathbf{r}, E)$ for points marked in (a). (e) The energy band of kink state in graphene around valley K.

by the nonequilibrium local density of states (DOS) [see Figs. 4(c) and 4(d) with the parameters marked in Fig. 4(a)]. It is calculated by $\rho(\mathbf{r}, E) = [\mathbf{G}^r \mathbf{\Gamma}_L \mathbf{G}^a]_{\mathbf{r}}/2\pi$, with $\mathbf{G}^{r/a}$ the Green function and $\mathbf{\Gamma}_L$ the linewidth function [30,32]. $\rho(\mathbf{r}, E)$ is large around the domain walls and is infinitesimal otherwise, indicating the good formation of the interferometer. Moreover, in Fig. 4(c) ($T_{13}^{\min}$), there is current flow into both terminals 2 and 3. In Fig. 4(d), the current flows into terminal 3 with terminal 2 blocked. So the interference of the valley current is well tuned by the magnetic field.

Figure 4(b) shows the T_{13} versus E relation when $B = 0$. T_{13} varies periodically, in analogy to Fig. 4(a), indicating that the Fermi level plays a similar role as that of a magnetic field, i.e., providing an extra phase. Physically the wave function is $\Psi(\boldsymbol{r}) = \Psi(r_\perp)e^{ik_\parallel l}$, with $k_\parallel$ the momentum. When $E = 0$, $k_\parallel$ is zero and the wave function gains no dynamic phase during the propagation (see Fig. S1 in Ref. [39]). However, when $E \neq 0$, $k_\parallel l$ contributes a phase to the wave function and changes the interference. Since the wave in the interferometer can only propagate clockwise, the extra phases of transmission amplitude acquired from the magnetic field and the Fermi level are similar. To explore the peaks' features of T_{13}, the local DOS of an isolated kink state circle [the blue path in Fig. 3(b)] is shown in Fig. 4(b). The peaks' positions of T_{13} and DOS are the same. It means the peaks of T_{13} result from the resonance tunneling through the kink state circle. Interestingly, we find that the zero energy is located in the middle of two peaks. It is from the π Berry phase of the kink state. The wave function of the kink state $\Psi(r_\perp)$ is made of two components (pseudospin), which bears the pseudospin-momentum locked topological nature [40]. After evolving along a closed circle, $\Psi(r_\perp)$ acquires a π Berry phase [39]. Thus, the Bohr-Sommerfeld quantization condition $k_\parallel l_0 = 2n\pi$ is modified to $k_\parallel l_0 = 2n\pi + \pi$ (l_0 is the circumference of the interferometer), which means no resonant peak is located at the zero energy. So the π Berry phase can be measured from the features of T_{13}. Additionally, the dispersion relation of the kink states can also be extracted from T_{13}. For example, in Fig. 4(b), there are n peaks from $E = 0$ to E_n and the corresponding momentum is $k_{\parallel,n} = (2n + 1)\pi/l_0$. In Fig. 4(e), the $E_n \sim k_{\parallel,n}$ relation is shown, in good agreement with the dispersion relation adopted from Fig. 2(c).

To clarify the above characteristics, the scattering matrix method is adopted [41,42]. At the left splitter, the amplitudes of the incident and outgoing waves are shown by a_1 or a_2 and c_1 or c_2, respectively [see Fig. 3(b)]. Assuming no backscattering, they are related by $(c_2, c_1)^T = S(a_1, a_2)^T$, with

$$S = \begin{pmatrix} \sqrt{1-\alpha}e^{-i\theta/2} & \sqrt{\alpha}e^{i(\pi-\theta)/2} \\ \sqrt{\alpha}e^{i(\pi-\theta)/2} & \sqrt{1-\alpha}e^{-i\theta/2} \end{pmatrix}$$

the scattering matrix. In S, $\sqrt{\alpha}$ and $\sqrt{1-\alpha}$ are the amplitudes of the wave function from terminal 1 to 2 and the upper arm of the interferometer, respectively. The Berry phase is also accounted in S, e.g. from a_1 to c_2, a phase of $e^{-i\theta/2}$ is acquired when the momentum direction rotates an angle θ anticlockwise. In the right splitter, $(c_3, a_2 e^{-i(\varphi+\theta)/2})^T = S(c_2 e^{i(\varphi+\theta)/2}, 0)^T$. Here, $\varphi = \phi + k_\parallel l_0$ is the combination of the magnetic phase and the dynamic phase. Finally, we have

$$T_{12}(\alpha,\varphi) = |c_1|^2 = \frac{4\alpha\cos^2\frac{\varphi}{2}}{(1-\alpha)^2 + 4\alpha\cos^2\frac{\varphi}{2}},$$
$$T_{13}(\alpha,\varphi) = |c_3|^2 = \frac{(1-\alpha)^2}{(1-\alpha)^2 + 4\alpha\cos^2\frac{\varphi}{2}}, \quad (2)$$

with $T_{12} + T_{13} = 1$ by using a_1 as a unit. The result is a Fabry-Perot-type interference and it comes from the multibeam interference. When $\varphi = 0$, T_{12} shows a maximum and T_{13} shows a minimum, the same as in Fig. 3. From the sample size in Fig. 3, we have $\theta \simeq 0.615\pi$, and it corresponds to $\alpha \simeq 0.22$ [see Fig. 2(c)]. By substituting this value into Eq. (2) and using $k_\parallel = 0$, the analytical results are displayed in Fig. 4(a), in good agreement with the numerical curve for $E = 0$. The small discrepancy at $\phi = \pi$ is due to the intervalley scattering at the intersections when the circulating current is large. This mechanism is omitted in the analytical approach.

The realization of monolayer graphene-based domain walls may be difficult in experiment. The Hamiltonian in Eq. (1) serves as a toy model to underline the nature of topological kink states conveniently. Recently, the topological kink states have been observed in classical wave graphene systems [8–14]. The physical picture behind it is the same as monolayer graphene. Thus our device, acting as a valleytronics prototype in classical wave graphene systems, can be fabricated under current experimental setups [8,14]. Similar to monolayer graphene, the topological kink states also exist in the line defect of MoS_2 [24], h-BN, etc. The experimental realization in these systems is also expected. Based on domain walls in topological insulators [1,2], the linear band structure and the π Berry phase can be obtained with our proposal.

Bilayer graphene interferometer.—From the technique aspect, kink state interferometers in bilayer graphene are more accessible in experiments [5,6,21–23,34]. In the following we investigate the Bernal-stacking bilayer graphene device. The model Hamiltonian is $H_b = H_m^{\text{top}} + H_m^{\text{bottom}} + \sum_{ij} t_\perp (c_i^\dagger c_j + c_j^\dagger c_i)$. It is constructed by the top and bottom layer of monolayer graphene [Eq. (1)] and the coupling in between. The spatial inversion asymmetry of bilayer graphene is induced by applying an electric field. In our model, it is accounted for by the on-site potential difference between two layers. In the blue (gray) region of Fig. 5(a), $\varepsilon_i = U(-U)$ in the upper layer and $\varepsilon_i = -U(U)$ in the bottom layer with $U = 0.1t$. The nearest coupling between two layers is $t_\perp = 0.15t$.

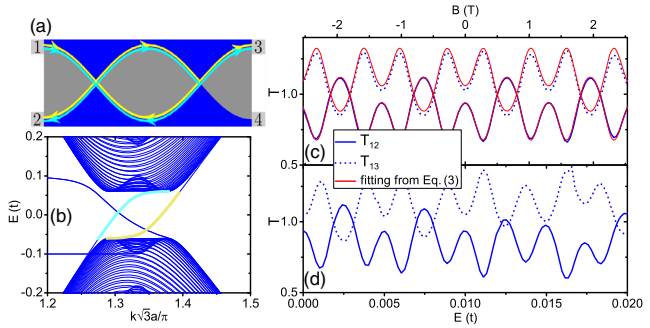

FIG. 5. (a) Schematics for wave propagation in bilayer graphene model. (b) Energy band of kink states in bilayer graphene around K point. T_{12} and T_{13} versus B (c) when $E = 0$ and versus E (d) when $B = 0$. The red curves are from Eq. (3).

Figure 5 plots the results for the bilayer graphene model. In Figs. 5(c) and 5(d), both T_{12} and T_{13} versus B show periodical oscillations and the period is the same as the case for the monolayer model because of the same sample sizes. In particular, T_{12}/T_{13}, proportional to the pure valley current in terminals 2 and 3, can be tuned for 1.68/1.53 times $[(T_{13}^{\max}/T_{13}^{\min})/(T_{12}^{\max}/T_{12}^{\min})]$. So the interference in bilayer graphene has promising application in valley current modulation as well. Different from the monolayer graphene model, which has only one period, T_{13} in Fig. 5(c) has two periods. It is ascribed to the double-kink states in the bilayer model [see Fig. 5(b)]. When $E = 0$, the phases of two kink states are $\varphi_\pm = \phi \pm k_\parallel^0 l$, including the same magnetic phase ϕ and nonzero dynamic phases with $\pm k_\parallel^0$ the momentum of two kink states. So T_{12} and T_{13} are the summation of two separate kink states' transmission. It can be directly obtained by using the scattering matrix method:

$$T_{12}(\alpha,\phi) = \frac{4\alpha\cos^2\frac{\varphi_+}{2}}{(1-\alpha)^2 + 4\alpha\cos^2\frac{\varphi_+}{2}} + \frac{4\alpha\cos^2\frac{\varphi_-}{2}}{(1-\alpha)^2 + 4\alpha\cos^2\frac{\varphi_-}{2}},$$
$$T_{13}(\alpha,\phi) = \frac{(1-\alpha)^2}{(1-\alpha)^2 + 4\alpha\cos^2\frac{\varphi_+}{2}} + \frac{(1-\alpha)^2}{(1-\alpha)^2 + 4\alpha\cos^2\frac{\varphi_-}{2}}. \quad (3)$$

In Fig. 5(c), the fitting curves from Eq. (3) are plotted ($\alpha = 0.28$ and $k_\parallel^0 l = 1.75$), in close agreement with the numerical results. From Eq. (3), two periods associated with $\varphi_\pm$ are clearly seen. The double-kink states in bilayer graphene have not been verified yet; e.g., the conductance is smaller than $4e^2/h$ [5,21]. Thus, our proposal can provide direct evidence to explore them. In addition, the two periods' oscillation exists in the presence of moderate disorder (see Fig. S5 in Ref. [39]). So the double-kink states

can be confirmed in experiment more easily with our proposal; i.e., no quantized conductance is required. Figure 5(d) shows the E dependence of T_{12} and T_{13} when $B = 0$. The two period feature still holds. But there exists an irregular oscillation pattern which should be ascribed to the nonlinear dispersion of kink states in bilayer graphene [see Fig. 5(b)]. Figure 5(d) also demonstrates that valley current can be tuned by the Fermi level in bilayer graphene. From Eqs. (2) and (3), the modulation of the valley current is dominated by the interference phase, so the above discussions hold true for interferometers of irregular shapes [34]. Additionally, the characterization of topological kink states in the above discussion is immune to the orientation of the nanoribbon [39].

In bilayer graphene, the desired domain wall structures are fabricated with electrostatic gating [3,23] or stacking line defects [34,35]. Our results for bilayer graphene can be realized under the current graphene techniques.

Conclusion.—In conclusion, an AB interferometer is proposed to characterize and manipulate the topological valley kink states. The output of the current is perfectly valley polarized and changes periodically in a large range when sweeping the Fermi energy or the magnetic field. It provides a versatile and efficient way to manipulate the valley degrees of freedom. For monolayer graphene, due to a single kink state, transmission coefficients have only one period. The π Berry phase and the linear band of the kink state can be extracted from the transport measurements. However, for the bilayer graphene, there are two kink states. The transmission coefficients modulated by a magnetic flux show two periods. Our proposal can also be used in experiments to characterize the topological nature of the kink states.

We thank L. He and Z. W. Shi for stimulating discussion. We also acknowledge the discussion with Z. H. Hang from the experimental aspect, and the related work is in progress. This work was supported by NSFC under Grants No. 11874298, No. 11822407, No. 11674264, No. 11534001, No. 11574007, and No. 11674028, NSF of Jiangsu Province, China (Grant No. BK20160007), National Key R and D Program of China (2017YFA0303301), NBRP of China (2015CB921102), and the Key Research Program of the Chinese Academy of Sciences (Grant No. XDPB08-4).

*jianghuaphy@suda.edu.cn
†sunqf@pku.edu.cn

[1] K. Yasuda, M. Mogi, R. Yoshimi, A. Tsukazaki, K. S. Takahashi, M. Kawasaki, F. Kagawa, and Y. Tokura, Quantized chiral edge conduction on domain walls of a magnetic topological insulator, Science **358**, 1311 (2017).
[2] I. T. Rosen, E. J. Fox, X. Kou, L. Pan, K. L. Wang, and D. Goldhaber-Gordon, Chiral transport along magnetic domain walls in the quantum anomalous Hall effect, npq Quantum Mater. **2**, 69 (2017).
[3] I. Martin, Y. M. Blanter, and A. F. Morpurgo, Topological Confinement in Bilayer Graphene, Phys. Rev. Lett. **100**, 036804 (2008).
[4] G. W. Semenoff, V. Semenoff, and F. Zhou, Domain Walls in Gapped Graphene, Phys. Rev. Lett. **101**, 087204 (2008).
[5] L. Ju, Z. W. Shi, N. Nair, Y. Lv, C. H. Jin, J. Velasco Jr., C. Ojeda-Aristizabal, H. A. Bechtel, M. C. Martin, A. Zettl, J. Analytis, and F. Wang, Topological valley transport at bilayer graphene domain walls, Nature (London) **520**, 650 (2015).
[6] L. J. Yin, H. Jiang, J. B. Qiao, and L. He, Direct imaging of topological edge states at a bilayer graphene domain wall, Nat. Commun. **7**, 11760 (2016).
[7] H. Pan, X. Li, F. Zhang, and S. Y. A. Yang, Perfect valley filter in a topological domain wall, Phys. Rev. B **92**, 041404 (R) (2015).
[8] J. Lu, C. Qiu, L. Ye, X. Fan, M. Ke, F. Zhang, and Z. Liu, Observation of topological valley transport of sound in sonic crystals, Nat. Phys. **13**, 369 (2017).
[9] X. X. Wu, Y. Meng, J. X. Tian, Y. Z. Huang, H. Xiang, D. Z. Han, and W. J. Wen, Direct observation of valley-polarized topological edge states in designer surface plasmon crystals, Nat. Commun. **8**, 1304 (2017).
[10] L. P. Ye, Y. T. Yang, Z. H. Hang, C. Y. Qiu, and Z. Y. Liu, Observation of valley-selective microwave transport in photonic crystals, Appl. Phys. Lett. **111**, 251107 (2017).
[11] J.-W. Dong, X.-D. Chen, H. Y. Zhu, Y. Wang, and X. Zhang, Valley photonic crystals for control of spin and topology, Nat. Mater. **16**, 298 (2017).
[12] J. Noh, S. Huang, K. P. Chen, and M. C. Rechtsman, Observation of Photonic Topological Valley Hall Edge States, Phys. Rev. Lett. **120**, 063902 (2018).
[13] Y. T. Yang, H. Jiang, and Z. H. Hang, Topological valley transport in two dimensional honeycomb photonic crystals, Sci. Rep. **8**, 1588 (2018).
[14] F. Gao, H.-r. Xue, Z.-j. Yang, K. Lai, Y. Yu, X. Lin, Y. Chong, G. Shvets, and B. L. Zhang, Topologically protected refraction of robust kink states in valley photonic crystals, Nat. Phys. **14**, 140 (2018).
[15] J. Jung, F. Zhang, Z. H. Qiao, and A. H. MacDonald, Valley-Hall kink and edge states in multilayer graphene, Phys. Rev. B **84**, 075418 (2011).
[16] A. Vaezi, Y. Liang, D. H. Ngai, L. Yang, and E.-A. Kim, Topological Edge States at a Tilt Boundary in Gated Multilayer Graphene, Phys. Rev. X **3**, 021018 (2013).
[17] F. Zhang, A. H. MacDonald, and E. J. Mele, Valley Chern numbers and boundary modes in gapped bilayer graphene, Proc. Natl Acad. Sci. U.S.A. **110**, 10546 (2013).
[18] X. Li, F. Zhang, Q. Niu, and A. H. MacDonald, Spontaneous Layer-Pseudospin Domain Walls in Bilayer Graphene, Phys. Rev. Lett. **113**, 116803 (2014).
[19] C. Lee, G. Kim, J. Jung, and H. Min, Zero-line modes at stacking faulted domain walls in multilayer graphene, Phys. Rev. B **94**, 125438 (2016).
[20] D. K. Efimkin and A. H. MacDonald, Helical network model for twisted bilayer graphene, Phys. Rev. B. **98**, 035404 (2018).

[21] J. Li, K. Wang, K. J. McFaul, Z. Zern, Y. F. Ren, K. Watanabe, T. Taniguchi, Z. H. Qiao, and J. Zhu, Gate-controlled topological conducting channels in bilayer graphene, Nat. Nanotechnol. **11**, 1060 (2016).

[22] L. L. Jiang, Z. W. Shi, B. Zeng, S. Wang, J. H. Kang, T. Joshi, C. H. Jin, L. Ju, J. Kim, T. Lyu, Y. R. Shen, M. Crommie, H. J. Gao, and F. Wang, Soliton-dependent plasmon reflection at bilayer graphene domain walls, Nat. Mater. **15**, 840 (2016).

[23] J. Li, R.-X. Zhang, Z. Yin, J. Zhang, K. Watanabe, T. Taniguchi, C. Liu, and J. Zhu, A valley valve and electron beam splitter in bilayer graphene, arXiv:1708.02311.

[24] A. Yan, C. S. Ong, D. Y. Qiu, C. Ophus, J. Ciston, C. Merino, S. G. Louie, and A. Zettl, Dynamics of symmetry-breaking stacking boundaries in bilayer MoS_2, J. Phys. Chem. C **121**, 22559 (2017).

[25] A. Rycerz, J. Tworzydło, and C. W. J. Beenakker, Valley filter and valley valve in graphene, Nat. Phys. **3**, 172 (2007).

[26] H. Pan, X. Li, H. Jiang, Y. G. Yao, and S. Y. A. Yang, Valley-polarized quantum anomalous Hall phase and disorder-induced valley-filtered chiral edge channels, Phys. Rev. B **91**, 045404 (2015).

[27] D. R. da Costa, A. Chaves, S. H. R. Sena, G. A. Farias, and F. M. Peeters, Valley filtering using electrostatic potentials in bilayer graphene, Phys. Rev. B **92**, 045417 (2015).

[28] S. G. Cheng, J. J. Zhou, H. Jiang, and Q-F. Sun, The valley filter efficiency of monolayer graphene and bilayer graphene line defect model, New J. Phys. **18**, 103024 (2016).

[29] S. G. Cheng, R. Z. Zhang, J. J. Zhou, H. Jiang, and Q. F. Sun, Perfect valley filter based on a topological phase in a disordered Sb monolayer heterostructure, Phys. Rev. B **97**, 085420 (2018).

[30] Z. H. Qiao, J. Jung, Q. Niu, and A. H. MacDonald, Electronic highways in bilayer graphene, Nano Lett. **11**, 3453 (2011).

[31] J. R. Anglin and A. Schulz, Analytical solutions of the two-dimensional Dirac equation for a topological channel intersection, Phys. Rev. B **95**, 045430 (2017).

[32] Z. H. Qiao, J. Jung, C. W. Lin, Y. F. Ren, A. H. MacDonald, and Q. Niu, Current Partition at Topological Channel Intersections, Phys. Rev. Lett. **112**, 206601 (2014).

[33] K. Wang, Y. F. Ren, X. Z. Deng, S. A. Yang, J. Jung, and Z. H. Qiao, Gate-tunable current partition in graphene-based topological zero lines, Phys. Rev. B **95**, 245420 (2017).

[34] L. L. Jiang, S. Wang, Z. W. Shi, C. H. Jin, M. I. B. Utama, S. H. Zhao, Y. R. Shen, H. J. Gao, G. Y. Zhang, and F. Wang, Manipulation of domain-wall solitons in bi- and trilayer graphene, Nat. Nanotechnol. **13**, 204 (2018).

[35] S. Q. Huang, K. Kim, D. K. Efimkin, T. Lovorn, T. Taniguchi, K. Watanabe, A. H. MacDonald, Emanuel Tutuc, and Brian J. LeRoy, Topologically Protected Helical States in Minimally Twisted Bilayer Graphene, Phys. Rev. Lett. **121**, 037702 (2018).

[36] W. Chen, W.-Y. Deng, J.-M. Hou, D. N. Shi, L. Sheng, and D. Y. Xing, π Spin Berry Phase in a Quantum-Spin-Hall-Insulator-Based Interferometer: Evidence for the Helical Spin Texture of the Edge States, Phys. Rev. Lett. **117**, 076802 (2016).

[37] S. Datta, *Electronic Transport in Mesoscopic Systems* (Cambridge University Press, Cambridge, England, 1995).

[38] T. Ando, Quantum point contacts in magnetic fields, Phys. Rev. B **44**, 8017 (1991).

[39] See Supplemental Material at http://link.aps.org/supplemental/10.1103/PhysRevLett.121.156801 for the role of the Fermi level (further verification), the deduction of the π Berry phase in an isolated kink state circle, the valley transport for a sample with different shape, different ribbon orientation, and the effects of disorder.

[40] S.-Q. Shen, *Topological Insulators, Dirac Equation in Condensed Matters*, Springer Series in Solid-State Sciences Vol. 174 (Springer, New York, 2013).

[41] M. Büttiker, Y. Imry, and M. Y. Azbel, Quantum oscillations in one-dimensional normal-metal rings, Phys. Rev. A **30**, 1982 (1984).

[42] Y. Gefen, Y. Imry, and M. Y. Azbel, Quantum Oscillations and the Aharonov-Bohm Effect for Parallel Resistors, Phys. Rev. Lett. **52**, 129 (1984).